Transonic Buffet in Flow Past a Low-Reynolds-Number Airfoil

Boyang Jia[1]; Weipeng Li[2]; and H. Jane Bae[3]

Abstract: For propeller-driven Mars airplanes operating at low Reynolds numbers, the speed of the rotor tips may reach transonic. To date, only a few studies have investigated the transonic buffet in flow past low-Reynolds-number airfoils. In this study, direct numerical simulations of high-speed flow ($M = 0.2$, 0.6, and 0.8) past a NACA 0012 airfoil are performed with a low Reynolds number of $Re_c = 23{,}000$, where transonic buffet is observed at $M = 0.8$. We first investigated the effects of Mach number on the aerodynamic performance and flow fields. Dynamic mode decomposition (DMD) and linear stability analysis (LSA) are used to analyze the flow instability mechanisms of the transonic buffet. Results showed that the multiple high-frequency oscillations are related to the vortex shedding at the trailing edge of the airfoil, and the low-frequency oscillation is caused by Type C shock motions. Both of them are confirmed to be self-sustained in feedback cycles. **DOI: 10.1061/JAEEEZ.ASENG-4978.** *© 2024 American Society of Civil Engineers.*

Introduction

The mission of airplanes on Mars has benefits of exploring and characterizing potential human landing sites and demonstrating approaches to precision landing and hazard avoidance. In order to produce sufficient lift, long-span propeller-driven Mars airplanes are mostly considered for these purposes (Oyama and Fujii 2013; Yonezawa et al. 2016; Koning et al. 2019, 2020). The flight conditions on Mars are unlike those encountered on Earth due to the lower atmospheric density and speed of sound, which lead to transonic aerodynamic effects at low Reynolds numbers (10^3 to 10^5), especially near the tip of the propeller blades. Therefore, it is of importance to understand the airfoil aerodynamics at such high-speed and low-Reynolds-number conditions.

At transonic flight conditions, the interaction between shock waves and boundary layer on airfoils may cause large-amplitude, low-frequency, autonomous shock oscillations, which are commonly known as transonic buffet (Lee 2001; Giannelis et al. 2017). Most previous studies (Bendiksen 2011; Hartmann et al. 2013; Fukushima and Kawai 2018, 2019) on transonic buffet focused on high Reynolds numbers to account for conditions on Earth. After the transonic buffet was first observed by Hilton and Fowler (1947), many researchers have paid attention to its physical mechanisms.

Tijdeman (1977) divided the shock oscillation into three types: (1) Type A, which consists of small-amplitude near-sinuous streamwise shock motion; (2) Type B, which is similar to Type A, but the amplitude of the streamwise oscillation is larger and the shock wave disappears in some phases within one cycle; and (3) Type C, which is fundamentally different from the previous two, has large-amplitude oscillations, and the main wave structure changes from compression waves to shock waves, then weakens to compression waves. Lee (1990) proposed a model to predict the self-sustained shock oscillation of the Type A motion, which was validated extensively (Lee 2001; Hartmann et al. 2013; Xiao et al. 2006). Nonetheless, some studies also argued that the Lee (1990) model exhibited discrepancies in predicting the buffet frequencies at different Reynolds numbers and airfoil geometries (Garnier and Deck 2010; Jacquin et al. 2009).

Iovnovich and Raveh (2012) studied the instability of the transonic buffet with Reynolds-averaged Navier–Stokes (RANS) simulations. They stated that the buffet onset is not related to the bursting of the separation bubble behind the shock (Pearcey 1958). They proposed that the wedge and dynamics effects increase the shock intensity as it moves upstream, whereas the airfoil surface curvature effect decreases the shock intensity as it moves upstream. Different from the turbulent regime, the laminar transonic buffet is associated with dynamics driven by vortex shedding (Brion et al. 2017) and the breathing dynamics of the laminar separation bubble under the shock foot (Dandois et al. 2018).

Brion et al. (2020) used two approaches, bumps and steady jet blowing, to suppress the transonic buffet efficiently. Zauner et al. (2023) reported that the frequency of the buffet is not sensitive to the Reynolds number, but the oscillating amplitude is increased as the Reynolds number decreases. Crouch et al. (2007, 2009a, b) suggested that transonic buffet is related to the instability of global aerodynamic modes. Crouch et al. (2019) used global stability analysis to investigate the onset of transonic buffet of infinite swept and unswept wings, and found that the buffeting-flow structure of swept wings is more complex than that on unswept wings.

Although many studies have focused on the transonic buffet at high Reynolds numbers, to date, very few works have investigated the features of the transonic buffet at low Reynolds numbers. At low Reynolds numbers, the effects of transition and laminar separation are crucial to airfoil performance (Huang and Lin 1995; Laitone 1997; Anyoji et al. 2014; Elawad and Eljack 2019). The conclusions for a transonic buffet obtained at high Reynolds numbers can not be directly extended to the structure at low Reynolds numbers because the types of buffet may differ at different Reynolds numbers (Giannelis et al. 2017; Bouhadji and Braza 2003a; Iovnovich and Raveh 2012). Numerical studies with

[1]Ph.D. Candidate, School of Aeronautics and Astronautics, Shanghai Jiao Tong Univ., Shanghai 200240, China. Email: jiaboyang@sjtu.edu.cn

[2]Professor, School of Aeronautics and Astronautics, Shanghai Jiao Tong Univ., Shanghai 200240, China (corresponding author). Email: liweipeng@sjtu.edu.cn

[3]Assistant Professor, Graduate Aerospace Laboratories, California Institute of Technology, Pasadena, CA 91125. ORCID: https://orcid.org/0000-0001-6789-6209. Email: jbae@caltech.edu

Note. This manuscript was submitted on November 17, 2022; approved on May 28, 2024; published online on August 14, 2024. Discussion period open until January 14, 2025; separate discussions must be submitted for individual papers. This paper is part of the ***Journal of Aerospace Engineering***, © ASCE, ISSN 0893-1321.

direct numerical simulation (DNS) (Hua et al. 2005; Bouhadji and Braza 2003a, b) and large-eddy simulation (LES) (Kojima et al. 2013; Almutairi et al. 2010, 2015) facilitated the counting of many efforts on flow dynamics of airfoils at low Reynolds numbers.

Sandberg et al. (2009) numerically studied the noise generation of flow past symmetrical NACA airfoils with different thicknesses and angles of attack at $M = 0.4$ and $Re_c = 50{,}000$, where Re_c is the Reynolds number based on the chord length c. Results showed that the modified theory of Amiet (1976) appears to be suitable for finite-thickness airfoils up to moderate incidence, but airfoil self-noise prediction based on surface pressure differences seems not to be generally applicable for higher angles of attack and thicker airfoil thicknesses.

In addition to studies on subsonic flow, there are also studies on transonic flow. Bouhadji and Braza (2003a) carried out the numerical simulation at the Mach number range 0.2–0.98 and a fixed Reynolds number of $Re_c = 1 \times 10^4$. They found that the flow is governed by two instability processes in the Mach number range 0.75–0.8, where, apart from the von Kármán mode instability, a lower-frequency mode appears due to the formation of weakly supersonic alternating zones in the region upstream of the airfoil, related to the buffeting phenomenon. Jones (2008) investigated the flow around the NACA 0012 at $Re_c = 1 \times 10^4$ by DNS, but did not observe the second low-frequency mode (Bouhadji and Braza 2003a). They found a low-frequency mode at higher Reynolds numbers, which is distinct from transonic buffet because it appears over $Re_c = 1 \times 10^4$ to 5×10^4 and $M = 0.2$–0.8. Kojima et al. (2020) performed resolvent analysis over a NACA 0012 and showed that with the appropriate forcing input, buffet can appear even at a Reynolds number of $Re_c = 2{,}000$.

Most studies on Mars aircraft were conducted at low Mach numbers, yet the rotor blades of Mars helicopters may reach transonic speeds at the tip regions. The objective of this study is to investigate the instability mechanism of transonic flow past a NACA 0012 airfoil at low Reynolds numbers, particularly focusing on the trailing-edge vortex shedding and transonic buffet phenomenon that occur simultaneously at low-Reynolds-number transonic conditions.

The paper is organized as follows. The section "Numerical Methods" describes the numerical methods and grid settings. The results of DNS and modal analysis of the transonic flow field are presented in the section "Results and Discussions." Unlike the subsonic case, both high- and low-frequency oscillations (i.e., trailing-edge vortex shedding and transonic buffet) are present in the transonic case. Dynamic mode decomposition (DMD) and local linear stability analysis (LSA) are applied to investigate the flow instability mechanisms. Finally, the section "Conclusions" summarizes the conclusions of this study.

Numerical Methods

Flow Conditions and Governing Equations

High-speed and low-Reynolds-number flow past a basic symmetric airfoil NACA 0012 is considered. Three simulations cases are performed with the free-stream Mach numbers being $M = 0.2$, 0.6, and 0.8, respectively. The Reynolds number Re_c based on the chord length c is fixed to be 23,000, and the angle of attack (AOA) is set to be 3.0°.

Kojima et al. (2013) reported that the two-dimensional DNS could obtain good agreement with the results of experiments and three-dimensional LES at Reynolds numbers less than 30,000. Lissaman (2003) also stated that when the Reynolds number is less than 30,000, the flow mainly consists of laminar flow. Thus, the governing equations to be solved are two-dimensional compressible Navier–Stokes equations

$$\frac{\partial \rho}{\partial t} + \frac{\partial}{\partial x_j}(\rho u_j) = 0 \tag{1}$$

$$\frac{\partial}{\partial t}(\rho u_i) + \frac{\partial}{\partial x_j}(\rho u_i u_j) = -\frac{\partial p}{\partial x_i} + \frac{1}{Re_c}\frac{q_j}{\partial x_j}\tau_{ij} \tag{2}$$

$$\frac{\partial e}{\partial t} + \frac{\partial}{\partial x_j}((e+p)u_j) = \frac{1}{Re_c}\frac{\partial}{\partial x_j}(\tau_{ij}u_i) - \frac{1}{Re_c}\frac{q_j}{\partial x_j} \tag{3}$$

where ρ = density; p = static pressure; e = total energy; and u_i ($i = 1, 2$) = velocities corresponding to the x_i direction. The variables are nondimensionalized by chord length c, free-stream speed of sound a_∞, density ρ_∞, and reference dynamic viscosity μ_∞. The static pressure p, viscous stress tensor τ_{ij}, heat flux vector q_j, and the sound speed a satisfy the following relations:

$$p = (\gamma - 1)\left(e - \frac{1}{2}\rho u_k u_k\right) \tag{4}$$

$$\tau_{ij} = 2\mu s_{ij} - \frac{2}{3}\mu \delta_{ij} s_{kk} \tag{5}$$

$$q_j = \frac{1}{(\gamma - 1)}\frac{\mu}{Pr}\frac{\partial a^2}{\partial x_j} \tag{6}$$

$$a = \sqrt{\gamma \frac{p}{\rho}} \tag{7}$$

where the specific heat ratio $\gamma = 1.4$; and the Prandtl number $Pr = 0.72$. The rate of strain tensor s_{ij} is expressed

$$s_{ij} = \frac{1}{2}\left(\frac{\partial u_i}{\partial x_j} + \frac{\partial u_j}{\partial x_i}\right) \tag{8}$$

The dynamic viscosity μ is determined by Sutherland's law as follows:

$$\mu = \frac{\mu^*}{\mu_\infty} = \left(\frac{T^*}{T_\infty}\right)^{\frac{3}{2}}\frac{T_\infty + C}{T^* + C} \tag{9}$$

where μ^* and T^* = dimensional viscosity and temperature, respectively; $C = 110.5$ K; $T_\infty = 273.1$ K; and $\mu_\infty = 1.716 \times 10^{-5}$ Pa · s.

Numerical Algorithm

The convective terms in the two-dimensional compressible Navier–Stokes equations are calculated with a modified seventh-order weighted compact nonlinear scheme (WCNS) (Nonomura and Fujii 2009; Nonomura et al. 2010, 2011). The viscous terms are employed with a sixth-order central differencing scheme. A second-order backward differencing converged by three subiterations of alternative direction implicit symmetric Gauss–Seidel (ADI-SGS) scheme (Nishida and Nonomura 2009) is implemented for the time integration, and the time step is chosen to ensure maximum Courant–Friedrichs–Lewy number to equal one, approximately. The in-house computational solver has been widely used for subsonic and supersonic flow simulations (Kojima et al. 2013, 2020; Nonomura and Fujii 2009; Nonomura et al. 2010, 2011; Chen et al. 2024; Zhang et al. 2016).

A C-shaped mesh is utilized, as shown in Fig. 1. The computational domain has an extent of $x_c/c \in [-100, 100]$ and $y_c/c \in [-100, 100]$, where x_c and y_c represent the lengths in the chordwise direction and chord-normal direction, respectively. The leading

J. Aerosp. Eng., 2024, 37(6): 04024082

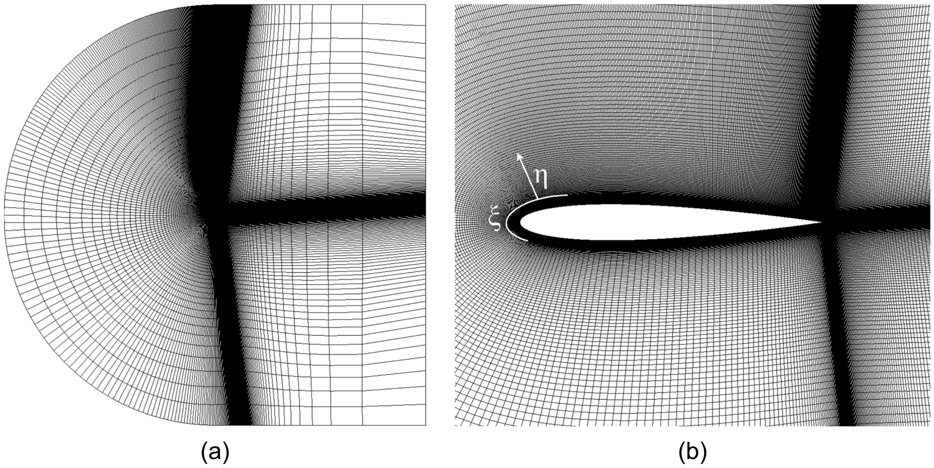

Fig. 1. Computational grid: (a) whole computational domain; and (b) grid around the airfoil.

Table 1. Grid resolutions

Grid	N_ξ	N_η	Total points
Grid-1	681	151	102,831
Grid-2	901	231	208,131
Grid-3	1,201	331	397,531

edge of the airfoil is located at the origin of the grid. We have densified the mesh around the airfoil surface and ensured that the grid satisfy the inequality $\Delta y^+ < 1$ and $\Delta x^+ < 10$, where Δ denotes the minimum grid spacing and a plus sign denotes a normalization based on viscous units. A nonslip adiabatic condition is applied to the wall surface, and a zero-gradient pressure condition is employed at the outer boundaries.

To examine the sufficiency of the grid resolution, a grid convergence study is conducted at $M = 0.8$ and $Re_c = 23{,}000$. Three meshes with different grid points in the wall-parallel (N_ξ) and wall-normal direction (N_η) are given in Table 1. The distribution of pressure coefficients simulated with three meshes are shown in Fig. 2(a), and the spectra of the lift coefficients are plotted in Fig. 2(b). No obvious difference was found in the distribution of pressure coefficients, and the frequencies and amplitude of the peaks in the spectra exhibited relatively small changes with the refinement of the grid resolution. Hereafter, we used the medium (Grid 2) mesh to analyze the flow fields.

Result and Discussions

Effects of Mach Number

We use all simulated cases ($M = 0.2$, 0.6, and 0.8) to discuss the effects of Mach number first. Figs. 3(a–c) show the variation of lift coefficients as a function of simulation time. The x-axis of the figure is the nondimensional time $t = t^* a_\infty / c$, where t^* is the dimensional time. It can be seen that when $t > 50$, the lift coefficients oscillate periodically and tend to be statistical stable. Therefore, the analyses hereafter only use the data in the range of $50 \leq t \leq 100$ unless otherwise mentioned.

It is obvious that the lift coefficients in the case of $M = 0.8$, as displayed in Fig. 3(c), oscillate differently from the other two cases. Fourier analyses were performed to check their oscillation modes by using fast Fourier transform (FFT). The FFT results are shown in

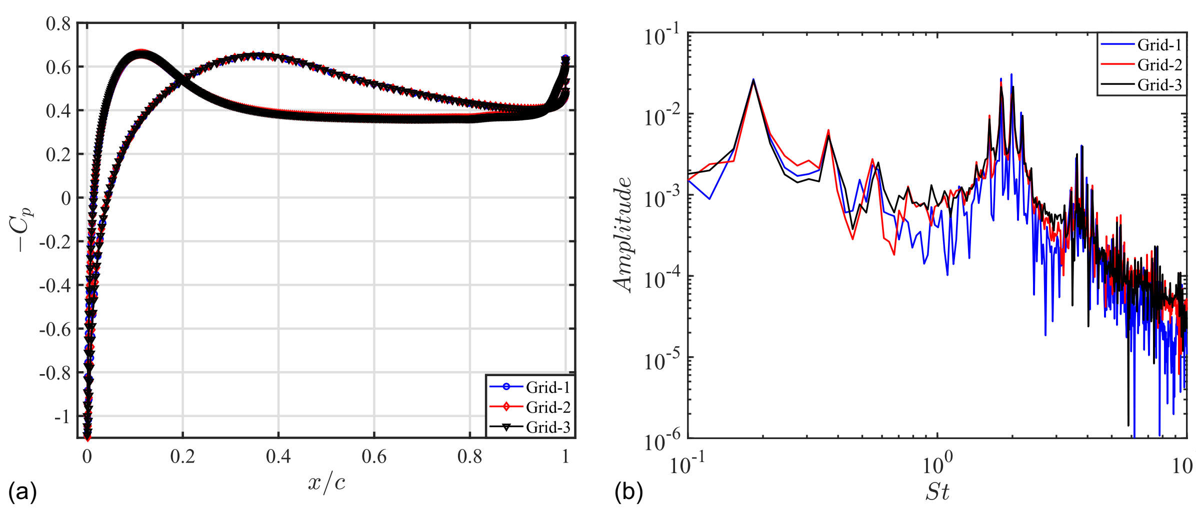

Fig. 2. Grid independence study: (a) distribution of time-averaged pressure coefficients; and (b) spectra of the lift coefficients at $M = 0.8$ and $Re_c = 23{,}000$.

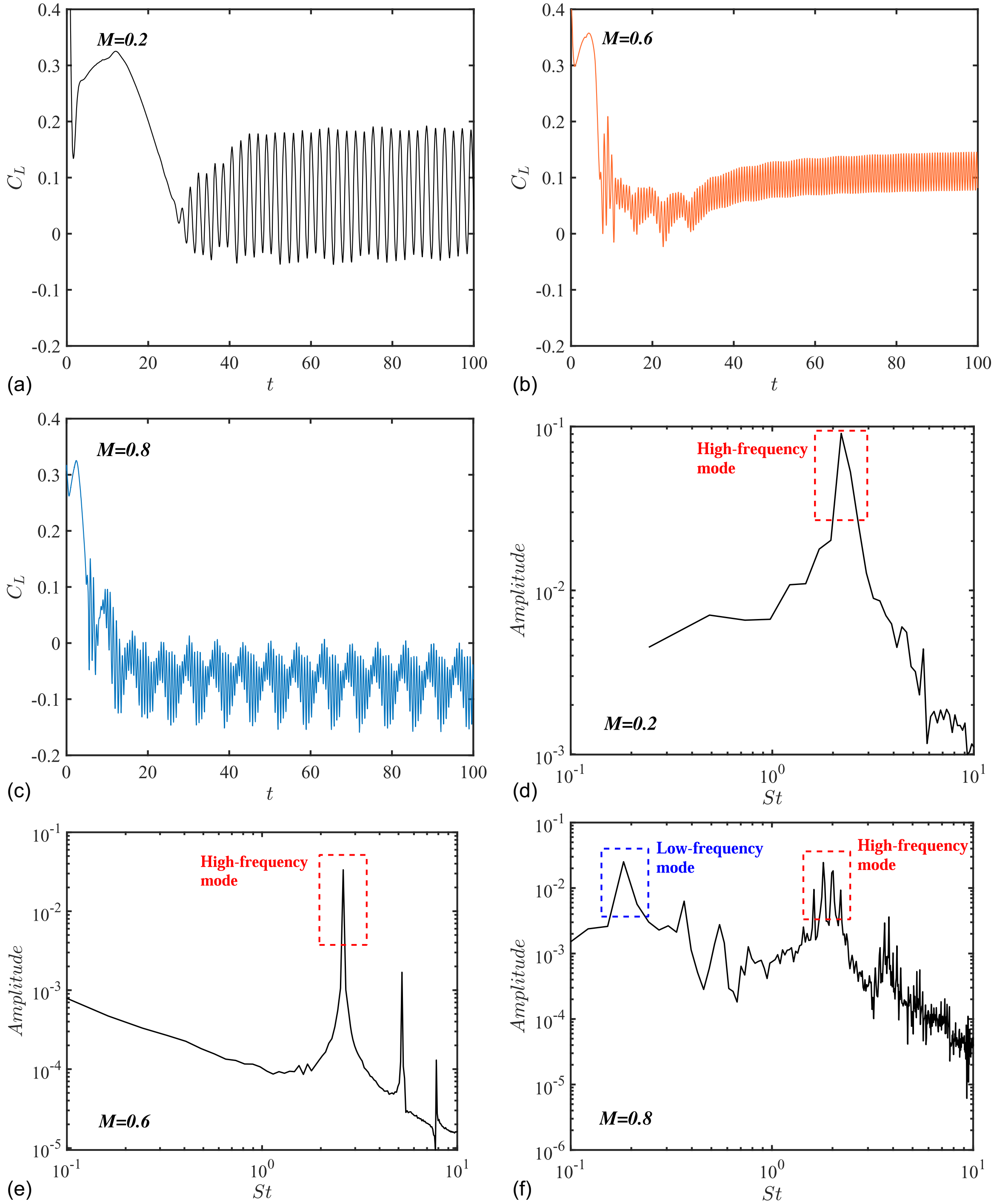

Fig. 3. (a–c) Variation of the lift coefficients as a function of time; and (d–f) spectra of the lift coefficients: (a and d) $M = 0.2$; (b and e) $M = 0.6$; and (c and f) $M = 0.8$.

Figs. 3(d–f). The Strouhal number is defined as $St = f^* c/U_\infty$, where f^* is the dimensional frequency. In the cases of $M = 0.2$ and 0.6, only one single mode is observed. Other peaks are harmonic modes. Whereas, in the case of $M = 0.8$, several high-frequency oscillation modes (not harmonic) are observed, coupling with a low-frequency oscillation mode.

Table 2 lists the frequencies of the peaks shown in Figs. 3(d–f). The frequencies of high-frequency modes are in the same order, approximately at $St \approx 2$. Unlike the other two cases, a low-frequency mode at $St = 0.1831$ exists in the case of $M = 0.8$.

Table 2. Frequencies of the low- and high-frequency oscillations at different Mach numbers

Mach number	High-frequency mode	Low-frequency mode
0.2	$St = 2.197$	—
0.6	$St = 2.604$	—
0.8	$St_1 = 1.617$ $St_2 = 1.801$ $St_3 = 2.014$ $St_4 = 2.197$	$St = 0.1831$

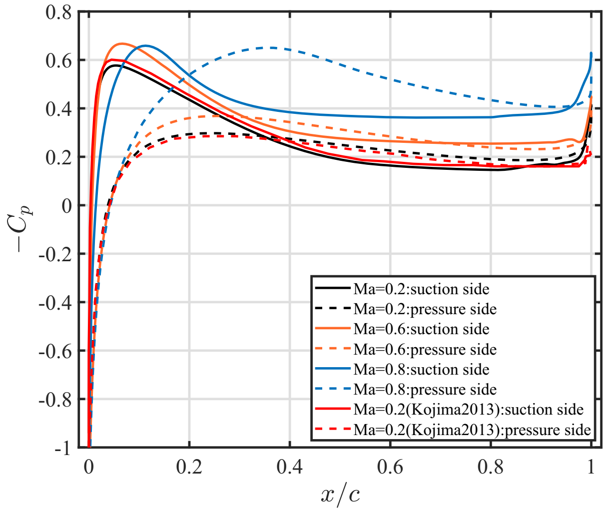

Fig. 4. Distributions of time-averaged pressure coefficients C_p.

This low-frequency mode is easily reminiscent of the transonic buffet.

Zauner et al. (2018) used DNS to simulate transonic flow past Dassault Aviation's V2C laminar wing at a moderate Reynolds number of $Re_c = 500{,}000$ and observed an obvious low-frequency cycle at $St \approx 0.12$. At high Reynolds numbers $Re_c = 3 \times 10^6$, the dominant buffet frequency in the studies of Jacquin et al. (2009) and Sartor et al. (2015) were found to be approximately $St \approx 0.07$. The reduced frequency of the low-frequency mode in the present study is similar to those mentioned previously, and we denote the low-frequency mode as the transonic buffet, which will be discussed subsequently.

As can be seen from Fig. 3(c), the lift coefficients in the case of $M = 0.8$ oscillate negatively, whereas the other two oscillate positively. This can be explained through the pressure coefficient, C_p. We show the distributions of the time-averaged pressure coefficients C_p around the airfoil in Fig. 4. The three-dimensional LES result (Kojima et al. 2013) at $M = 0.2$ and $Re_c = 23{,}000$ is also shown in Fig. 4 to validate our result at the same conditions. It can be seen that the predictions of C_p at $M = 0.2$ are consistent with the results of three-dimensional LES result by Kojima et al. (2013). As Mach number increases, the distribution of C_p at $M = 0.6$ is similar to that at $M = 0.2$; but at $M = 0.8$, the negative integrate C_p in the range of $0.2 \leq x/c \leq 1$ overcomes the positive one, which leads to the negative lift coefficients.

Fig. 5 displays the contours of the time-averaged Mach number. Solid lines in Fig. 5(c) bound the regions of supersonic flow, covering about 20% and 60% in regions of suction and pressure side, respectively. For all cases, leading-edge separation existed on the suction side of the airfoil. As Mach number increased, the mean separation point moved upstream, from $x = 0.42$ at $M = 0.2$ to $x = 0.32$ at $M = 0.6$, and $x = 0.25$ at $M = 0.8$. The leading-edge separation reached the trailing-edge of the airfoil without reattachment. As the Mach number increased, the flow separation on the suction side became increasingly severe. Consequently, the pressure differences on the suction and pressure side of the airfoil became more evident, as displayed in Fig. 4, which is possible related to the occurrence of negative lift.

Contours of dynamical fluctuations $\{(1/2)[(u_x')^2 + (u_y')^2]\}$ are shown in Fig. 6. High-amplitude values were observed near the trailing-edge of the airfoil, which is related to the formation of vortical structures periodically shedding from the trailing edge. Unlike the other two cases, notable dynamical fluctuations were detected in the shear layer separated from the leading-edge of the airfoil at transonic conditions. It indicates that the shear layer oscillates upward and downward due to the interaction with the upstream-propagating shock wave.

Because there have been many papers on the cases of subsonic flow fields at low Reynolds numbers (Kojima et al. 2013; Anyoji et al. 2014, 2015; Aono et al. 2020), next we will focus on the transonic case only.

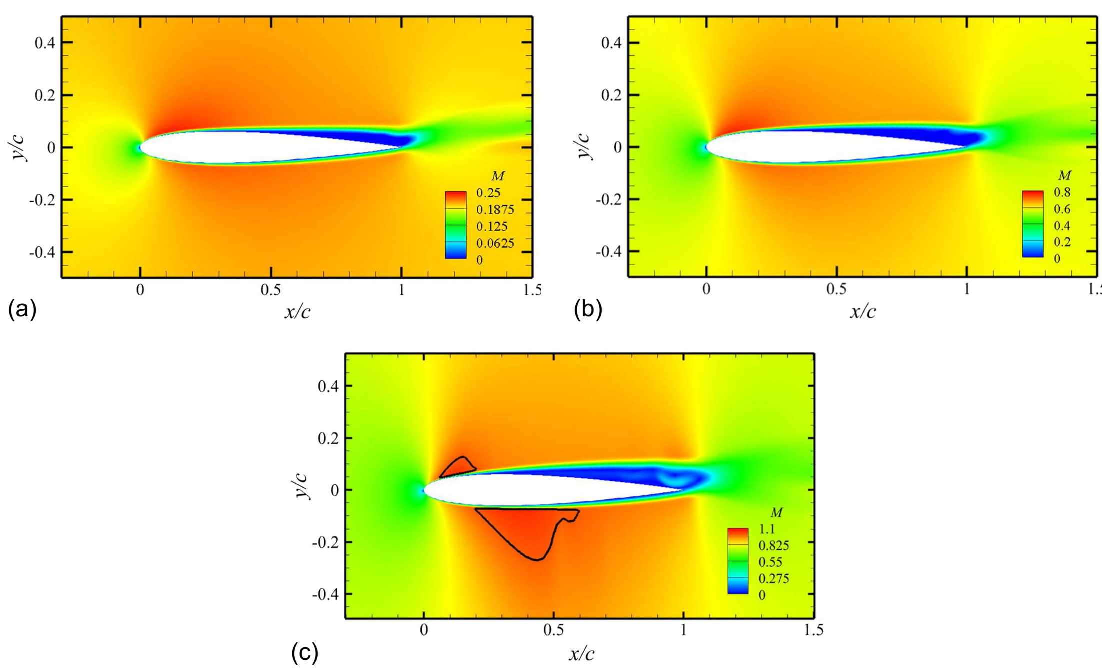

Fig. 5. Contours of time-averaged Mach number: (a) $M = 0.2$; (b) $M = 0.6$; and (c) $M = 0.8$. Solid lines in plot (c) denote the sonic lines.

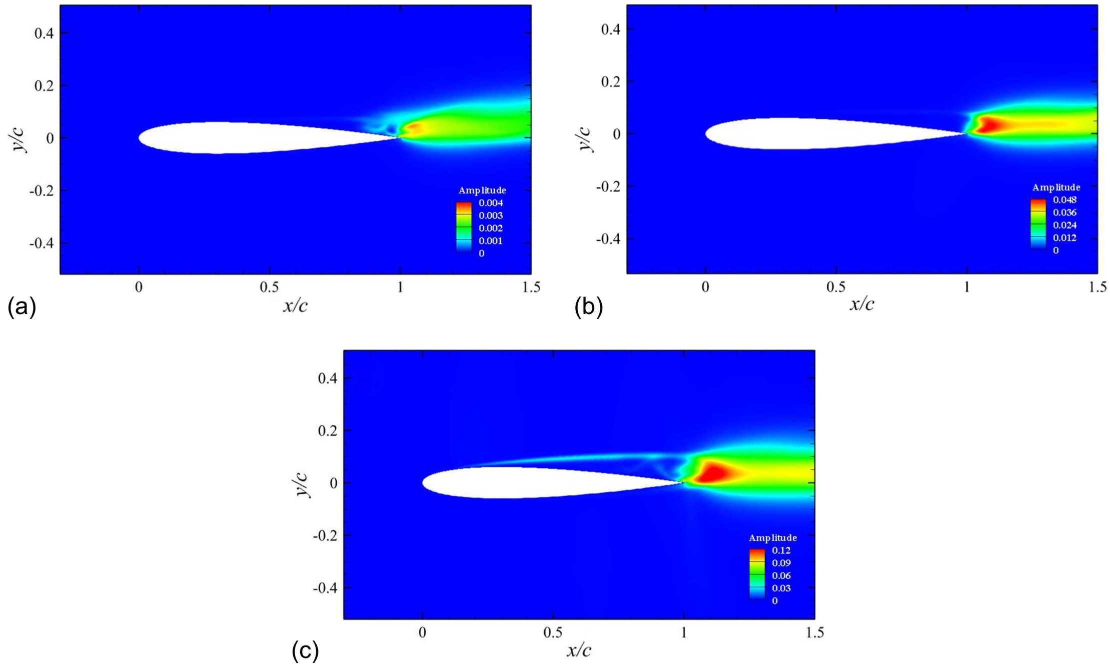

Fig. 6. Contours of dynamical fluctuations in the cases of (a) $M = 0.2$; (b) $M = 0.6$; and (c) $M = 0.8$.

Type C Shock Motion at $M = 0.8$

Hereafter, we will focus on the transonic buffet in the case of $M = 0.8$. Tijdeman (1977) divided the shock motion into three types according to the amplitude and dynamic motions of the shock waves. For the Type C shock motion, it is described that compression waves, which generate on the suction side of the airfoil, accumulate to form shock waves. The shock waves propagate upstream and leave the leading edge of the airfoil without downstream (backward) motions. The self-sustained formation and leaving of the shock waves dramatically impact the flow dynamics and aerodynamic performances of the airfoil.

The low-frequency mode observed in this study is regarded to be associated with the Type C shock motion, and we describe the shock motions in Fig. 7 by using the contours of the density gradients. The snapshots of four representative phases were chosen corresponding to one low-frequency oscillation cycle of C_L in Fig. 3(c).

Compression waves coalescing to form a shock wave near the leading edge were taken as the initial phase. As shown in Fig. 7(a), in the initial stage, the flow field distortion due to the vortex shedding generates compression waves near the trailing edge of the airfoil, which move upstream and coalesce near the supersonic region. The line in the figure represents the sonic line, and CW denotes compression waves. The compression waves coalesced gradually near the supersonic region and increased the intensity, forming a shock wave, indicated by SW in Fig. 7(b).

In Figs. 7(c and d), the shock wave intensified and moved upstream, eventually exiting from leading edge of the airfoil and going back to the initial phase in Fig. 7(a). There was no downstream motion of the shock wave, and this process repeats periodically. According to the category by Tijdeman (1977), the low-frequency shock motions observed in this study belong to the Type C shock motion. Unlike the Type C shock motion mentioned by Tijdeman (1977), the pressure side did not exhibit shock oscillations. This could be attributed to the fact that Tijdeman (1977)'s investigation were conducted at an angle of attack AOA $= 0°$, whereas ours were performed at AOA $= 3°$, resulting in the absence of alternating shock oscillations on the suction and pressure sides.

Dynamic Mode Decomposition

DMD is used to analyze the dynamics in the case of $M = 0.8$. Details of the DMD algorithm can be found in previous studies (Schmid and Sesterhenn 2010; Jonathan et al. 2014; Kutz et al. 2016). In total, 3,001 snapshots of instantaneous pressure fields, containing at least eight low-frequency oscillation cycles of the lift coefficients, were employed for the DMD analysis. The spectrum of the DMD results is shown in Fig. 8. The energy is normalized by the maximum amplitude. The low-frequency mode and high-frequency modes are all marked. Recalling the C_L oscillations in Fig. 3(f), we compare their peak frequencies with the DMD observations, which are listed in Table 3. Good agreements of the peak frequencies indicate that DMD has captured the resultant dynamic features of the unsteady flow fields.

The low-frequency DMD mode at $St = 0.1874$ is displayed in Fig. 9, exhibiting differences from the Type A buffet modes observed in high Reynolds number flows (Poplingher and Raveh 2023). Distinct wave patterns were observed ahead of the airfoil. The wavelength is about $\lambda \approx 1.4c$, which corresponds to a frequency of $f^* = (a_0 - U_\infty)/\lambda$, and consequently, $St \approx 0.18$, when the wave propagates upstream with speed of $a_0 - U_\infty$. The pattern ahead of the airfoil is expected to be the compression waves related to the upstream propagation and attenuation of shock waves. It indicates that the flow oscillations in the near region of the airfoil are able to impact the pressure fields of the incoming flow.

A pair of strong-amplitude regions appears in the wake of the airfoil, which may be related to the periodic interactions of the shock waves with the separated shear-layer on the suction side of the airfoil. Furthermore, the flow oscillations in the wake and upper side of the airfoil are coupling with significant dynamics on the lower side of the airfoil, which is also seen in Fig. 7. The wave patterns in the low-frequency DMD mode provide more evidence for the Type C shock motion, that is, the shock waves

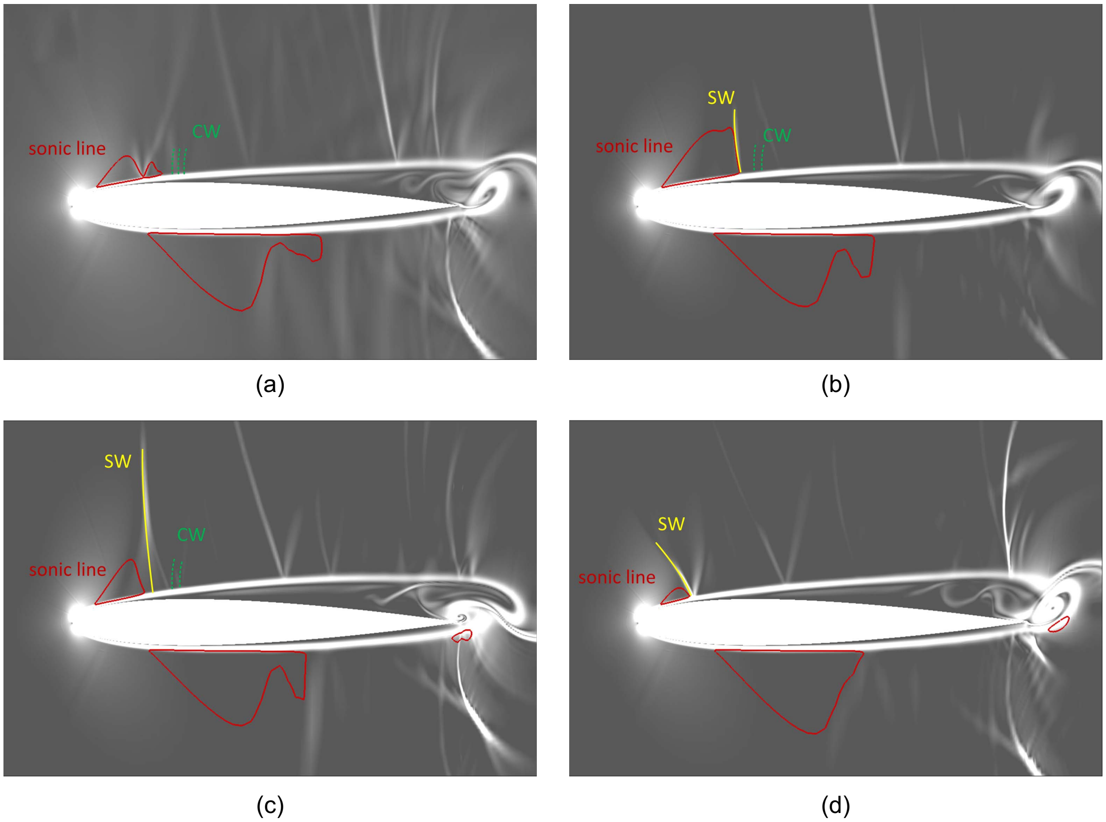

Fig. 7. Shock motions illustrated by contours of density gradients: (a) $\phi = 0(2\pi)$; (b) $\phi = (\pi/2)(5\pi/2)$; (c) $\phi = \pi(3\pi)$; and (d) $\phi = (3\pi/2)(7\pi/2)$. SW = shock waves, and CW = compression waves.

formed near the leading edge propagate upstream and eventually leave the leading edge of the airfoil to generate weak compression waves in the incoming flow. There may exist a self-sustained feedback mechanism between shock motions and instabilities in the separated boundary layer (Lee 1990), which will be discussed in next subsection.

Four high-frequency DMD modes are shown in Fig. 10. Firstly, unlike the low-frequency mode, the wave patterns are mostly constrained near the trailing edge of the airfoil, indicating direct

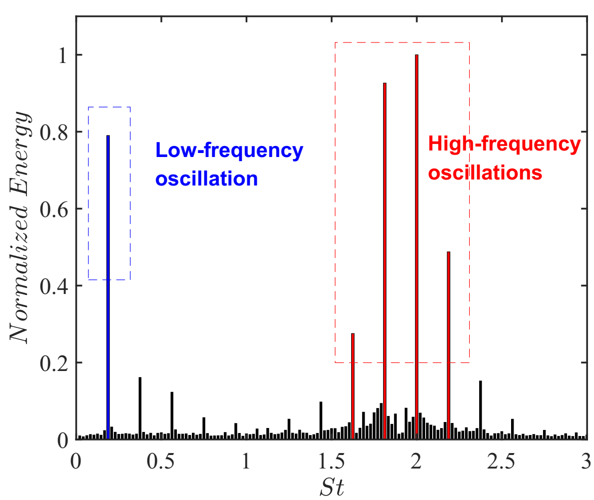

Fig. 8. Spectrum of the DMD analysis.

Table 3. Frequencies of the low- and high-frequency oscillations using DMD and FFT methods

Method	Low-frequency mode	High-frequency modes
DMD method	$St = 0.1874$	$St_1 = 1.625$ $St_2 = 1.812$ $St_3 = 1.999$ $St_4 = 2.187$
FFT method	$St = 0.1831$	$St_1 = 1.617$ $St_2 = 1.801$ $St_3 = 2.014$ $St_4 = 2.197$

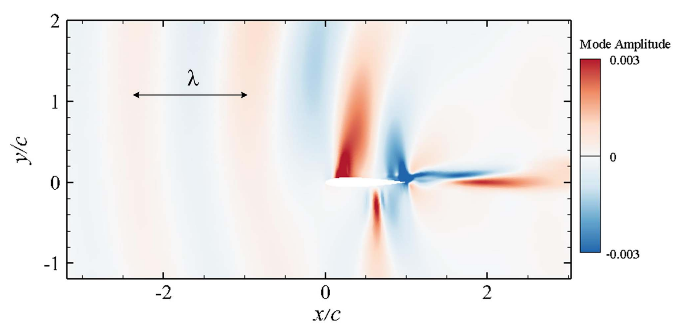

Fig. 9. Spatial distributions of the low-frequency DMD eigenmode.

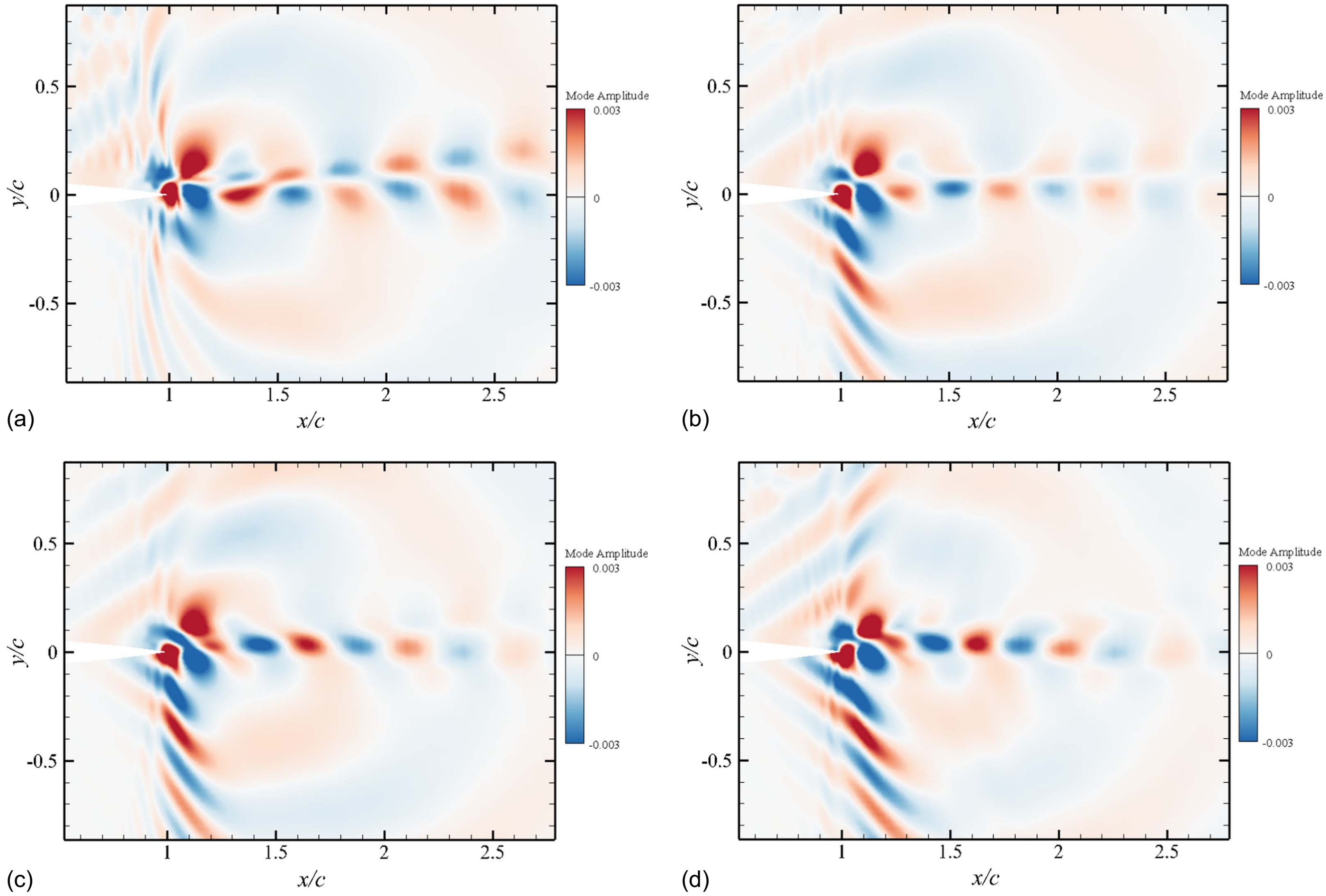

Fig. 10. Spatial distributions of high-frequency DMD eigenmodes at (a) $St = 1.625$; (b) $St = 1.812$; (c) $St = 1.999$; and (d) $St = 2.187$.

linkage to the classical trailing-edge vortex shedding in low-Reynolds-number airfoils. Regarding the multiple high-frequency modes exhibited by vortex shedding, Zhang et al. (2016) performed two-dimensional DNS of flow ($M = 0.2$ and $Re = 1 \times 10^4$ and 5×10^4) past a NACA 0012 airfoil. They observed that multiple modes are detected in the higher-Reynolds-number cases, but only one single tone in the cases at $Re = 1 \times 10^4$. They reported that all modes are driven by the instabilities in the separated boundary layer, which governing the formation of the trailing-edge vortex shedding.

The vortical structures near the trailing edge are complex, and we integrate the vorticity magnitude along a wall-normal straight line from wall surface to $0.1c$ at the station of $x/c = 0.9$ on the upper side of the airfoil

$$\Omega(t) = \int_{s=0}^{s=0.1c} |\omega(t)| \mathrm{d}s \tag{10}$$

where $|\omega(t)|$ = instantaneous vorticity magnitude; and s = length of the straight line. The spectrum of the signal Ω is shown in Fig. 11. It can be seen that the peak frequencies at $St = 0.183$, 1.648, 1.831, 2.014, and 2.197 in Fig. 11 are identical with the frequencies in the DMD spectrum, both in the low- and high-frequency regimes. It suggests that the vortex shedding is highly affected by the instabilities of the separated boundary layer. In the next subsection, we will apply LSA to explore the instabilities in the separated boundary layer.

Linear Stability Analysis

The flow quantity q can be divided into a base flow $\bar{q}$ and a small-amplitude perturbation q' (i.e., $\|q'\|/\|\bar{q}\| \ll 1$) via Reynolds' decomposition. We assumed that the base flow $\bar{q} = \bar{q}(\eta)$ is steady and homogeneous (periodic in space) in the direction parallel to the wall surface, and then the perturbation can be written

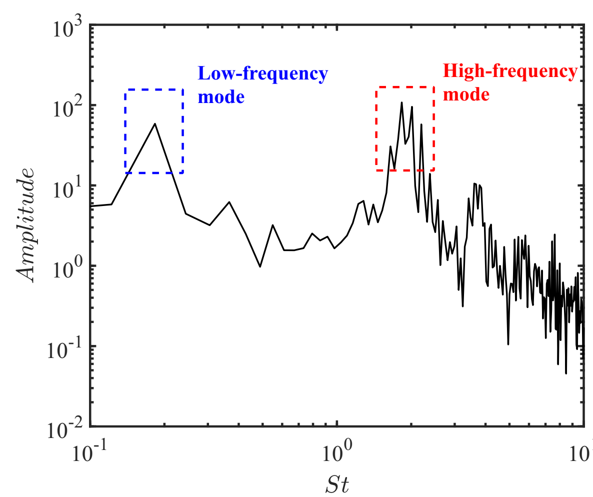

Fig. 11. Spectrum of the signal Ω.

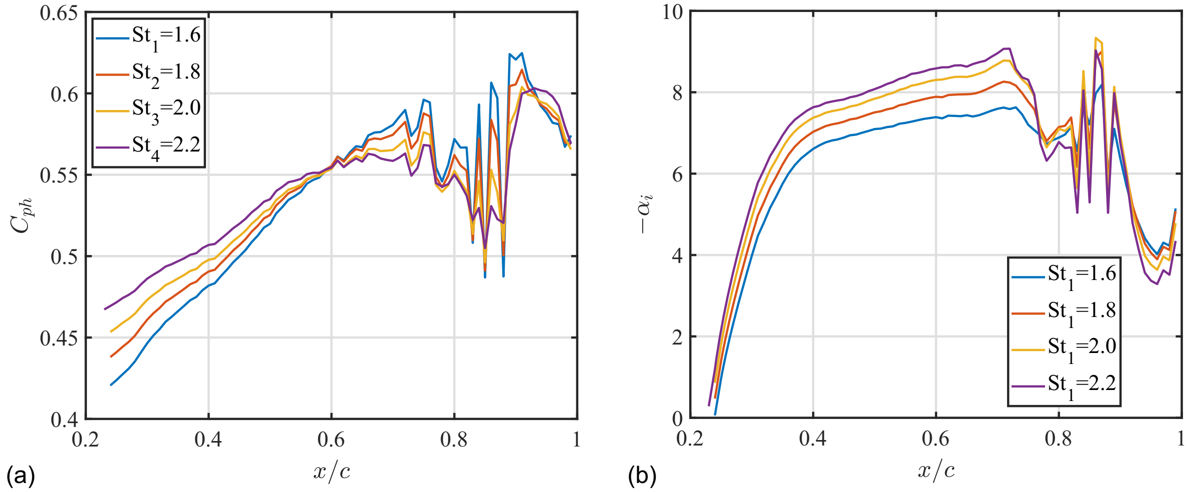

Fig. 12. (a) Phase speed C_{ph}; and (b) spatial growth rate α_i of the unstable modes on the upper side of the airfoil.

$$q'(\xi,\eta,t) = \hat{q}(\eta)e^{\mathrm{i}(\alpha\xi-\omega t)} + c.c. \tag{11}$$

where ω = angular frequency; and $c.c.$ = complex conjugate. The real and imaginary components of the complex number $\alpha = \alpha_r + \mathrm{i}\alpha_i$ correspond to the wave number and growth rate of the amplitude function $\hat{q}(y)$ of such frequency.

Substituting the flow quantity $q = \bar{q} + q'$ into the Navier–Stokes equations and neglecting the quadratic terms of the perturbation, we can obtain the linearized Navier–Stokes equations written in matrix form as follows:

$$\mathbf{A}(\bar{q};\omega)\hat{q} = \alpha\mathbf{B}\hat{q} \tag{12}$$

where the matrix $\mathbf{A}$ depends on the base flow $\bar{q}$ and the angular frequency ω, and the matrix $\mathbf{B}$ is invertible for the compressible flow (Taira et al. 2017). The complex number α can be calculated by solving a generalized eigenvalue problem.

The time-averaged flow is treated as base flow. We picked positions from the leading edge to the trailing edge with $\Delta x = 0.1c$ and made ω equal to the angular frequency of the high- and low-frequency oscillations. The variations of the spatial growth rate α_i at different positions and angular frequency are shown in Figs. 12(b) and 14(c). It can be seen that positive growth rates ($-\alpha_i > 0$) occurred at $x/c > 0.2$, which basically overlapped the flow separation regions with the separation point at $x/c = 0.25$. This satisfies that the boundary layer becomes unstable when inflectional velocity profiles appear (Schmid and Henningson 2001).

The feedback mechanism may drive the trailing-edge vortex shedding and acoustic radiation (Tam 1974; Arbey and Bataille 1983; Arcondoulis et al. 2012; Kingan and Pearse 2009). We explored the feedback mechanism with the mathematical model proposed by Kingan and Pearse (2009) as follows:

$$\frac{1}{2\pi}\int_b^a \alpha_r^*(s)\mathrm{d}s + \frac{1}{2} + \frac{f^*L}{a_0 - U_{\infty,L}} = n, \quad (n = 1,2,3,\dots) \tag{13}$$

Laminar boundary-layer instabilities, known as Tollmien–Schlichting waves (T-S waves) (Schlichting 1968), become amplified as they move over the airfoil surface. In the feedback loop, unstable T-S waves generated at $s = a$ propagate downstream at phase speed C_{ph}. The vortices generated by T-S waves pass over the trailing edge ($s = b$) and emit sound waves. Then, the sound waves propagate upstream and disturb the boundary layer to induce new T-S waves. According to Arbey and Bataille (1983), the noise radiation at the trailing edge has a 180° (π rad) phase shift from the T-S waves. The model assumes that the feedback loop will be sustained when the total phase change is a multiple of 2π. The feedback loop mechanism facilitates our exploration of high-frequency oscillations modes.

The quantities superscripted with an asterisk in Eq. (13) are dimensional, unless otherwise stated; the quantities without asterisks in the following are nondimensional after being normalized by freestream velocity and chord length. The relationship between the angular frequency ω and the nondimensional frequency f follows $\omega = 2\pi f$, and the phase speed is calculated with $C_{ph} = \omega/\alpha_r$. Dividing both sides of the Eq. (13) by the frequency, the first term is mainly related to the phase speed of the unstable waves propagating downstream. By selecting high frequencies at $St = 1.6$, 1.8, 2.0, and 2.2, in Fig. 12(a), we plot the variation of the phase speed C_{ph} on the upper side of the airfoil.

The trends of C_{ph} were similar at the four selected frequencies. It gradually increased from the separation point to the trailing edge of the airfoil, with large fluctuation at $0.82 < x/c < 0.88$. Fig. 12(b) shows the distribution of the growth rate of the high-frequency modes. It was observed that T-S waves emerged approximately at station $x/c = 0.23$; growth rates kept increasing downstream and fluctuated considerably near the trailing edge. We substituted the frequencies and phase speeds into Eq. (13) and plotted the theoretical predications with the DNS results in Fig. 13.

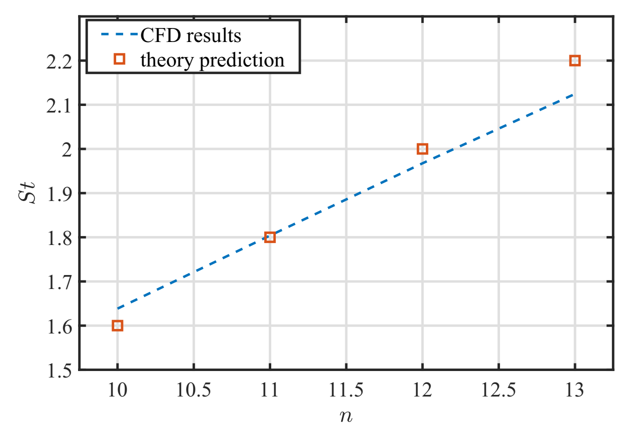

Fig. 13. Model predictions against DNS results.

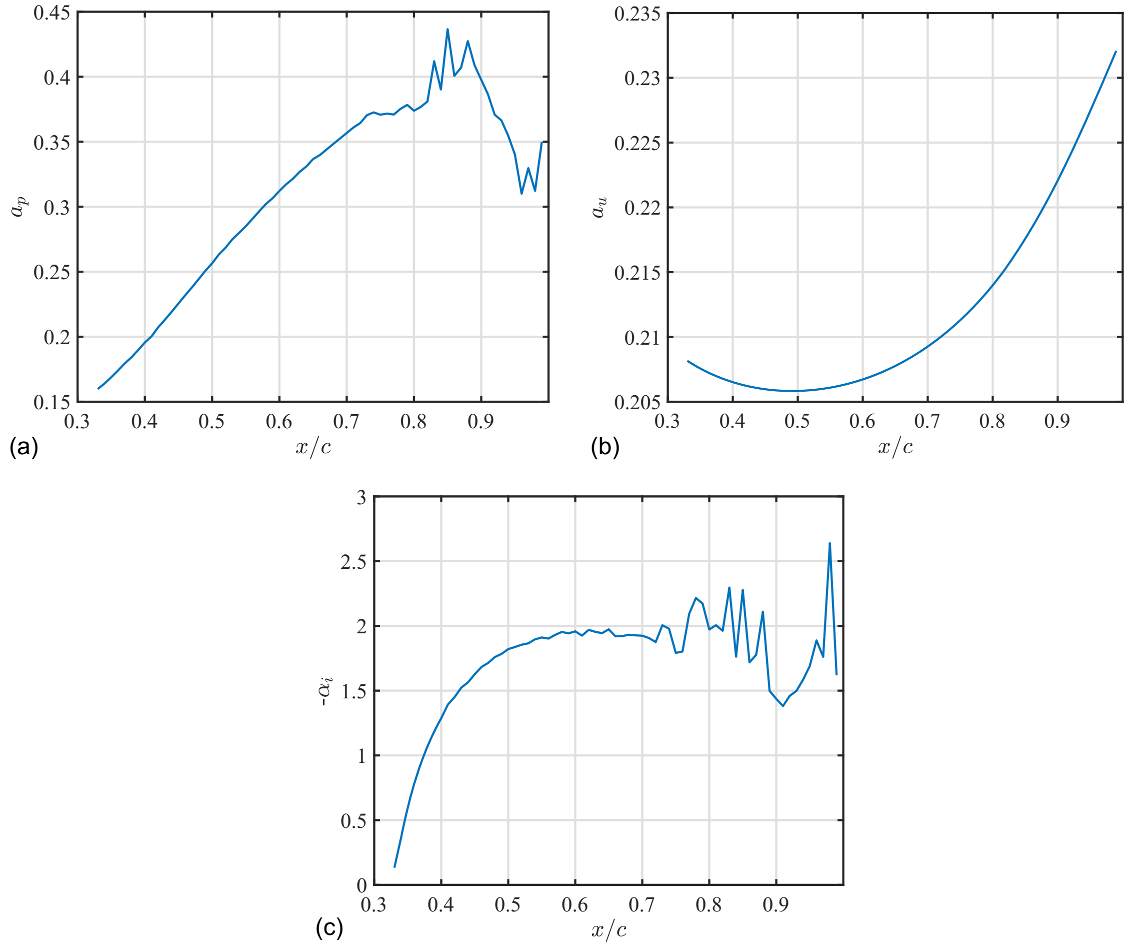

Fig. 14. (a) Downstream propagating speed α_p; (b) upstream propagating speed α_u of the pressure waves on the upper side of the airfoil; and (c) spatial growth rate α_i of the unstable modes on the upper side of the airfoil.

Good agreements were observed, which confirms that the high-frequency oscillations are governed by the feedback mechanism (Tam 1974; Arbey and Bataille 1983; Arcondoulis et al. 2012; Kingan and Pearse 2009).

Regarding the low-frequency buffet mode, Lee (1990) proposed a mechanism of self-sustained shock oscillations (Tijdeman 1977). The shock wave moves periodically on the upper surface of the airfoil and forms pressure waves within the boundary layer, which propagate downstream with speed of a_p. When the pressure waves reach the trailing edge, new waves are generated and propagate upstream with speed of a_u. They will interact with the shock wave and impart energy to maintain its oscillation. It implies that the period of the shock-wave oscillation should agree with the time it takes for a disturbance to propagate from the shock to the trailing edge plus the duration for an upstream moving wave to reach the shock from the trailing edge via the region outside the separated flow (Lee 1990). Lee (1990) proposed a model to predict the period of shock motions as follows:

$$T_p = \int_{x_s}^{c} 1/a_p \mathrm{d}x - \int_{c}^{x_s} 1/a_u \mathrm{d}x \tag{14}$$

where $a_u = (1 - M_{\mathrm{loc}})a_{\mathrm{loc}}$, where $M_{\mathrm{loc}} = R[M_{\mathrm{loc|s}} - M] + M$, where M_{loc} and a_{loc} are the local Mach number and speed of sound, respectively, and R is a relaxation factor varying between zero and one. We take $R = 0.7$, according to the experimental study (Lee 2001).

The phase speed of wave propagation can be obtained from the LSA results at the frequency corresponding to the low-frequency buffet. In addition, the position of the first appearance of low-frequency instability (i.e., $-\alpha_i > 0$) can be also obtained by LSA. We found that the position is close to the supersonic region, where shock waves start to form, and treated it as the shock position [i.e., x_s in Eq. (14)]. We show the a_p and a_u at different positions in Fig. 14.

Take the inverse of the speeds in Fig. 14 and integrate them along the transverse coordinate x/c. The integration was applied by the trapezoid method to obtain the time required for the two processes of propagating downstream and upstream, respectively. As a result, the Strouhal number required for the whole process of shock motion was $St = 0.1855$, which is very close to the DNS observation at $St = 0.1831$. The difference between the prediction and the DNS result is acceptable because it has assumptions and uncertainties in the LSA. Although the model proposed by Lee (1990) is suitable for Type A self-sustained shock oscillation, it is also applicable to the Type C shock motion under the current flow conditions.

Conclusions

We performed DNS of flow past a NACA 0012 airfoil at three Mach numbers ($M = 0.2$, 0.6, and 0.8) and a fixed Reynolds number at $Re_c = 23{,}000$, aiming to investigate the flow instabilities of high-speed low-Reynolds-number Mars airplanes. Results showed that lift coefficients at $M = 0.2$ and $M = 0.6$ have only one high-frequency oscillation mode, whereas at $M = 0.8$, a low-frequency mode ($St \approx 0.2$) appears, coupling with several multiple high-frequency modes ($1.6 < St < 2.2$). The high-frequency oscillations are related to the vortex shedding at the trailing edge of the airfoil (i.e., Kármán vortex street), and the low-frequency oscillation is caused by the motion of the shock waves (i.e., transonic buffet).

By using phase-locked snapshots and DMD analysis, we found that the low-frequency oscillation belongs to the Type C shock motion, in which the shock waves formed near the tailing edge of the airfoil propagate upstream and leave the leading edge of the airfoil without downstream (backward) motions. The self-sustained formation and leaving of the shock waves dramatically impact the flow dynamics and aerodynamic performances of the airfoil. Linear stability analysis was used to explore the instabilities in the separated boundary layer at the identified frequencies and verified the feedback mechanism. Results suggest that both the high-frequency trailing-edge vortex shedding and low-frequency shock motions are self-sustained in feedback cycles, which were well-predicted with the model of Kingan and Pearse (2009) and Lee (1990), respectively.

The results of this study indicate that the low-frequency buffet is a critical factor influencing the aerodynamic performance. The adoption of thin airfoil profiles with increased camber may suppress boundary-layer separation and mitigate the buffet. Furthermore, breaking the feedback loops of buffet may be achieved by adopting trip devices placed ahead of the boundary-layer separation point. Finally, reducing the rotor diameter and increasing the rotor quantity are able to prevent blade tip speeds from reaching transonic conditions, as observed in multirotor aircraft. We hope that this study can benefit the understanding and future rotor design of Mars helicopters.

Data Availability Statement

Some or all data, models, or code generated or used during the study are proprietary or confidential in nature and may only be provided with restrictions.

Acknowledgments

The funding support of the National Natural Science Foundation of China (Grant No. 12372221) is acknowledged.

References

Almutairi, J., I. Alqadi, and E. Eljack. 2015. "Large eddy simulation of a NACA-0012 airfoil near stall." In *Direct and Large-Eddy simulation IX*, 389–395. Cham, Switzerland: Springer.

Almutairi, J. H., L. E. Jones, and N. D. Sandham. 2010. "Intermittent bursting of a laminar separation bubble on an airfoil." *AIAA J.* 48 (2): 414–426. https://doi.org/10.2514/1.44298.

Amiet, R. K. 1976. "Noise due to turbulent flow past a trailing edge." *J. Sound Vib.* 47 (3): 387–393. https://doi.org/10.1016/0022-460X(76)90948-2.

Anyoji, M., T. Nonomura, H. Aono, A. Oyama, K. Fujii, H. Nagai, and K. Asai. 2014. "Computational and experimental analysis of a high-performance airfoil under low-Reynolds-number flow condition." *J. Aircr.* 51 (6): 1864–1872. https://doi.org/10.2514/1.C032553.

Anyoji, M., D. Numata, H. Nagai, and K. Asai. 2015. "Effects of Mach number and specific heat ratio on low-Reynolds-number airfoil flows." *AIAA J.* 53 (6): 1640–1654. https://doi.org/10.2514/1.J053468.

Aono, H., K. Kondo, T. Nonomura, M. Anyoji, and M. Yamamoto. 2020. "Aerodynamics of owl-like wing model at low Reynolds numbers." *Trans. Jpn. Soc. Aeronaut. Space Sci.* 63 (1): 8–17. https://doi.org/10.2322/tjsass.63.8.

Arbey, H., and J. Bataille. 1983. "Noise generated by airfoil profiles placed in a uniform laminar flow." *J. Fluid Mech.* 134 (1): 33–47. https://doi.org/10.1017/S0022112083003201.

Arcondoulis, E. J. G., C. J. Doolan, L. A. Brooks, and A. C. Zander. 2012. "On the generation of airfoil tonal noise at zero angle of attack and low to moderate Reynolds number." In *Proc., 18th AIAA/CEAS Aeroacoustics Conf. (33rd AIAA Aeroacoustics Conf.)*. Reston, VA: American Institute of Aeronautics and Astronautics.

Bendiksen, O. O. 2011. "Review of unsteady transonic aerodynamics: Theory and applications." *Prog. Aerosp. Sci.* 47 (2): 135–167. https://doi.org/10.1016/j.paerosci.2010.07.001.

Bouhadji, A., and M. Braza. 2003a. "Organised modes and shock-vortex interaction in unsteady viscous transonic flows around an aerofoil: Part I: Mach number effect." *Comput. Fluids* 32 (9): 1233–1260. https://doi.org/10.1016/S0045-7930(02)00100-7.

Bouhadji, A., and M. Braza. 2003b. "Organised modes and shock–vortex interaction in unsteady viscous transonic flows around an aerofoil: Part II: Reynolds number effect." *Comput. Fluids* 32 (9): 1261–1281. https://doi.org/10.1016/S0045-7930(02)00101-9.

Brion, V., J. Dandois, J. Abart, and P. Paillart. 2017. "Experimental analysis of the shock dynamics on a transonic laminar airfoil." *Prog. Flight Phys.* 9 (9): 365–386.

Brion, V., J. Dandois, R. Mayer, P. Reijasse, T. Lutz, and L. Jacquin. 2020. "Laminar buffet and flow control." *Proc. Inst. Mech. Eng. Part G: J. Aerosp. Eng.* 234 (1): 124–139. https://doi.org/10.1177/0954410018824516.

Chen, B., X. Qiang, F. Wu, M. Yang, and W. Li. 2024. "Implicit large-eddy simulation of an over-expanded screeching rectangular jet." *Chinese J. Aeronaut.* https://doi.org/10.1016/j.cja.2024.03.015.

Crouch, J. D., A. Garbaruk, and D. Magidov. 2007. "Predicting the onset of flow unsteadiness based on global instability." *J. Comput. Phys.* 224 (2): 924–940. https://doi.org/10.1016/j.jcp.2006.10.035.

Crouch, J. D., A. Garbaruk, D. Magidov, and L. Jacquin. 2009a. "Global structure of buffeting flow on transonic airfoils." In *Proc., IUTAM Symp. on Unsteady Separated Flows and their Control*, 297–306. Berlin: Springer.

Crouch, J. D., A. Garbaruk, D. Magidov, and A. Travin. 2009b. "Origin of transonic buffet on aerofoils." *J. Fluid Mech.* 628 (Jun): 357–369. https://doi.org/10.1017/S0022112009006673.

Crouch, J. D., A. Garbaruk, and M. Strelets. 2019. "Global instability in the onset of transonic-wing buffet." *J. Fluid Mech.* 881 (Dec): 3–22. https://doi.org/10.1017/jfm.2019.748.

Dandois, J., I. Mary, and V. Brion. 2018. "Large-eddy simulation of laminar transonic buffet." *J. Fluid Mech.* 850 (Sep): 156–178. https://doi.org/10.1017/jfm.2018.470.

Elawad, Y. A., and E. M. Eljack. 2019. "Numerical investigation of the low-frequency flow oscillation over a NACA-0012 aerofoil at the inception of stall." *Int. J. Micro Air Veh.* 11 (Apr): 1–17. https://doi.org/10.1177/1756829319833687.

Fukushima, Y., and S. Kawai. 2018. "Wall-modeled large-eddy simulation of transonic airfoil buffet at high Reynolds number." *AIAA J.* 56 (6): 2372–2388. https://doi.org/10.2514/1.J056537.

Fukushima, Y., and S. Kawai. 2019. "Self-sustained shock-wave oscillation mechanisms of transonic airfoil buffet." In *Proc., AIAA Scitech Forum*. Reston, VA: American Institute of Aeronautics and Astronautics.

Garnier, E., and S. Deck. 2010. "Large-eddy simulation of transonic buffet over a supercritical airfoil." In *Proc., Seventh Int. ERCOFTAC Workshop on Direct and Large-Eddy Simulation VII, held at the University of Trieste*, 549–554. Cham, Switzerland: Springer.

Giannelis, N. F., G. A. Vio, and O. Levinski. 2017. "A review of recent developments in the understanding of transonic shock buffet." *Prog. Aerosp. Sci.* 92 (Jul): 39–84. https://doi.org/10.1016/j.paerosci.2017.05.004.

Hartmann, A., A. Feldhusen, and W. Schröder. 2013. "On the interaction of shock waves and sound waves in transonic buffet flow." *Phys. Fluids* 25 (2): 026101. https://doi.org/10.1063/1.4791603.

Hilton, W. F., and R. G. Fowler. 1947. *Photographs of shock wave movement. NPL R&M No. 2692*. New Delhi, India: National Physical Laboratories.

Hua, S., J. Li, and C. Liu. 2005. "Direct numerical simulation of flow separation around a NACA 0012 airfoil." *Comput. Fluids* 34 (9): 1096–1114. https://doi.org/10.1016/j.compfluid.2004.09.003.

Huang, R. F., and C. L. Lin. 1995. "Vortex shedding and shear-layer instability of wing at low-Reynolds numbers." *AIAA J.* 33 (8): 1398–1403. https://doi.org/10.2514/3.12561.

Iovnovich, M., and D. E. Raveh. 2012. "Reynolds-averaged Navier-Stokes study of the shock-buffet instability mechanism." *AIAA J.* 50 (4): 880–890. https://doi.org/10.2514/1.J051329.

Jacquin, L., P. Molton, S. Deck, B. Maury, and D. Soulevant. 2009. "Experimental study of shock oscillation over a transonic supercritical profile." *AIAA J.* 47 (9): 1985–1994. https://doi.org/10.2514/1.30190.

Jonathan, H. T., W. R. Clarence, M. L. Dirk, L. B. Steven, and J. N. Kutz. 2014. "On dynamic mode decomposition: Theory and applications." *J. Comput. Dyn.* 1 (2): 391–421. https://doi.org/10.3934/jcd.2014.1.391.

Jones, L. E. 2008. "Numerical studies of the flow around an airfoil at low Reynolds number." Doctoral dissertation, School of Engineering Sciences, Univ. of Southampton.

Kingan, M. J., and J. R. Pearse. 2009. "Laminar boundary layer instability noise produced by an aerofoil." *J. Sound Vib.* 322 (4–5): 808–828. https://doi.org/10.1016/j.jsv.2008.11.043.

Kojima, R., T. Nonomura, A. Oyama, and K. Fujii. 2013. "Large-Eddy simulation of low-Reynolds-number flow over thick and thin NACA airfoils." *J. Aircr.* 50 (1): 187–196. https://doi.org/10.2514/1.C031849.

Kojima, Y., C. A. Yeh, K. Taira, and M. Kameda. 2020. "Resolvent analysis on the origin of two-dimensional transonic buffet." *J. Fluid Mech.* 885 (Feb): R1. https://doi.org/10.1017/jfm.2019.992.

Koning, W. J., E. A. Romander, and W. Johnson. 2020. "Optimization of low Reynolds number airfoils for Martian rotor applications using an evolutionary algorithm." In *Proc., AIAA Scitech Forum*. Reston, VA: American Institute of Aeronautics and Astronautics.

Koning, W. J. F., W. Johnson, and H. F. Grip. 2019. "Improved mars helicopter aerodynamic rotor model for comprehensive analyses." *AIAA J.* 57 (2): 1–10. https://doi.org/10.2514/1.J058045.

Kutz, J. N., S. L. Brunton, B. W. Brunton, and J. L. Proctor. 2016. *Dynamic mode decomposition: Data-driven modeling of complex systems*. Philadelphia: Society for Industrial and Applied Mathematics.

Laitone, E. V. 1997. "Wind tunnel tests of wings at Reynolds numbers below 70 000." *Exp. Fluids* 23 (5): 405–409. https://doi.org/10.1007/s003480050128.

Lee, B. H. K. 1990. "Oscillatory shock motion caused by transonic shock boundary-layer interaction." *AIAA J.* 28 (5): 942–944. https://doi.org/10.2514/3.25144.

Lee, B. H. K. 2001. "Self-sustained shock oscillations on airfoils at transonic speeds." *Prog. Aerosp. Sci.* 37 (2): 147–196. https://doi.org/10.1016/S0376-0421(01)00003-3.

Lissaman, P. B. S. 2003. "Low-Reynolds-number airfoils." *Annu. Rev. Fluid Mech.* 15 (1): 223–239. https://doi.org/10.1146/annurev.fl.15.010183.001255.

Nishida, H., and T. Nonomura. 2009. "ADI-SGS scheme on ideal magnetohydrodynamics." *J. Comput. Phys.* 228 (9): 3182–3188. https://doi.org/10.1016/j.jcp.2009.01.032.

Nonomura, T., and K. Fujii. 2009. "Effects of difference scheme type in high-order weighted compact nonlinear schemes." *J. Comput. Phys.* 228 (10): 3533–3539. https://doi.org/10.1016/j.jcp.2009.02.018.

Nonomura, T., N. Iizuka, and K. Fujii. 2010. "Freestream and vortex preservation properties of high-order WENO and WCNS on curvilinear grids." *Comput. Fluids* 39 (2): 197–214. https://doi.org/10.1016/j.compfluid.2009.08.005.

Nonomura, T., W. Li, Y. Goto, and K. Fujii. 2011. "Efficiency improvements in seventh-order weighted compact nonlinear scheme." *CFD J.* 18 (2): 180–186.

Oyama, A., and K. Fujii. 2013. "A study on airfoil design for future Mars airplane." In *Proc., 44th AIAA Aerospace Sciences Meeting and Exhibit*. Reston, VA: American Institute of Aeronautics and Astronautics.

Pearcey, H. H. 1958. *A method for the prediction of the onset of buffeting and other separation effects from wind tunnel tests on rigid models*. Paris: North Atlantic Treaty Organization, Advisory Group for Aeronautical Research and Development.

Poplingher, L., and D. E. Raveh. 2023. "Comparative modal study of the two-dimensional and three-dimensional transonic shock buffet." *AIAA J.* 61 (1): 125–144. https://doi.org/10.2514/1.J061797.

Sandberg, R. D., L. E. Jones, N. D. Sandham, and P. F. Joseph. 2009. "Direct numerical simulations of tonal noise generated by laminar flow past airfoils." *J. Sound Vib.* 320 (4–5): 838–858. https://doi.org/10.1016/j.jsv.2008.09.003.

Sartor, F., C. Mettot, and D. Sipp. 2015. "Stability, receptivity, and sensitivity analyses of buffeting transonic flow over a profile." *AIAA J.* 53 (7): 1980–1993. https://doi.org/10.2514/1.J053588.

Schlichting, H. 1968. *Boundary layer theory.* 6th ed. Berlin: Springer.

Schmid, P. J., and D. S. Henningson. 2001. *Stability and transition in shear flows*. New York: Springer.

Schmid, P. J., and J. Sesterhenn. 2010. "Dynamic mode decomposition of numerical and experimental data." *J. Fluid Mech.* 656 (10): 5–28. https://doi.org/10.1017/S0022112010001217.

Taira, K., S. L. Brunton, S. T. M. Dawson, C. W. Rowley, T. Colonius, B. J. Mckeon, O. T. Schmidt, S. Gordeyev, V. Theofilis, and L. S. Ukeiley. 2017. "Modal analysis of fluid flows: An overview." *AIAA J.* 55 (12): 4013–4041. https://doi.org/10.2514/1.J056060.

Tam, C. K. W. 1974. "Discrete tones of isolated airfoils." *J. Acoust. Soc. Am.* 55 (6): 1173–1177. https://doi.org/10.1121/1.1914682.

Tijdeman, H. 1977. *Investigations of the transonic flow around oscillating airfoils*. Amsterdam, Netherlands: National Aerospace Lab.

Xiao, Q., H. M. Tsai, and L. Feng. 2006. "A numerical study of transonic buffet on a supercritical airfoil." *AIAA J.* 44 (3): 620–628. https://doi.org/10.2514/1.16658.

Yonezawa, K., K. Abe, and S. Sunada. 2016. "Propeller design and loss mechanisms in low-Reynolds-number flows." *J. Propul. Power* 32 (6): 1378–1385. https://doi.org/10.2514/1.B35854.

Zauner, M., N. De Tullio, and N. D. Sandham. 2018. "Direct numerical simulations of transonic flow around an airfoil at moderate Reynolds numbers." *AIAA J.* 57 (2): 597–607. https://doi.org/10.2514/1.J057335.

Zauner, M., P. Moise, and N. Sandham. 2023. "On the co-existence of transonic buffet and separation-bubble modes for the OALT25 laminar-flow wing section." *Flow Turbul. Combust.* 110 (4): 1023–1057. https://doi.org/10.1007/s10494-023-00415-4.

Zhang, Y., X. Wu, and W. Li. 2016. "Direct numerical simulations of tonal noise generation for a two dimensional airfoil at low and moderate Reynolds numbers." In *Proc., 46th AIAA Fluid Dynamics Conf*. Reston, VA: American Institute of Aeronautics and Astronautics.

J. Aerosp. Eng., 2024, 37(6): 04024082